Simulation of Quantum Current in Double Gate MOSFETs: Vortices in Electron Transport

Pratik B. Vyas*, Maarten L. Van de Put†, and Massimo V. Fischetti†
*Department of Electrical and Computer Engineering, †Department of Materials Science and Engineering
The University of Texas at Dallas, 800 W. Campbell Rd., Richardson, Texas 75080, USA

***Abstract*—Quantum simulation of electronic transport in double gate (DG) field-effect transistors (FETs) and FinFETs is usually deemed to be required as the devices are scaled to the nanometer length-scale. Here, we present results obtained using a simulation program to model ballistic quantum transport in these devices. Our quantum simulations show the presence of quasi bound electronic states in the channel and Fano-interference phenomenon in the transport behavior of ultra-thin body (UTB) Si DG MOSFETs. Vortices in electron wavefunctions are also reported at energies at which transmission zeros (antiresonance) occur.**

***Index Terms*—Fano antiresonance, quantum interference, electron transport, DG MOSFET, Schrödinger, QTBM.**

I. Introduction

Ultra-thin body (UTB) double gate (DG) MOSFETs have a strong potential to overcome short channel effects [1] and thus have superior scalability in comparison to conventional MOSFETs. Moreover, these device structures provide a significant improvement in performance [2] in terms of low subthreshold slope, high ON current and high switching speed. This makes them very attractive for current and near future generations of silicon (Si) semiconductor devices. Simulation of these devices is usually done using semi-classical approaches based on the solution of Boltzmann transport equation (BTE) [3], [4], moments of BTE [5] or compact models augmented by quantum corrections [6], [7]. However, a full quantum treatment of these devices is necessary, since at such small dimensions explicit quantum effects would become observable. We present here a simulation tool, based on the effective mass approximation, to model two-dimensional (2-D) ballistic quantum transport in these devices. To this end, we determine the 2-D self-consistent solution of the Schrödinger and Poisson equations with *open* boundary conditions using the popular Quantum Transmitting Boundary method (QTBM) [8].

The most striking result that we obtain is the occurrence of the Fano-interference phenomenon [9] in the simulated UTB DG FETs. Bowen *et al.* [10] have shown that the Fano resonance-antiresonance line shapes can be accurately represented by poles and zeros, respectively, of the inverse of the retarded Green's function representing the system Hamiltonian (tight-binding, in their study) connected to infinite reservoirs. They have presented an efficient numerical method, based on a shift-and-invert non-symmmetric (SINS) Lanczos algorithm, to locate the poles and zeros, mentioned above, in single-barrier GaAs/AlAs/GaAs heterostructures. Fano interference has also been previously predicted and/or experimentally reported in the optical absorption spectra of impurities in crystals [11], quantum waveguides [12], and coupled quantum dot systems [13], [14]. Our observation of this resonance in a realistic CMOS device structure thus presents a novel and interesting case. Additionally, the simulated device exhibits only symmetric antiresonance 'dips' in electron transmission, contrary to the characteristic asymmetric Fano resonance-antiresonance line-shape observed in all the former cases. Moreover, vortices in current density are seen at energies at which antiresonance occurs. Such vortices have been previously reported in quantum simulations of semiconductor devices, but only in the presence of deviations from ideality – scattering with discrete dopant atoms [15] or tapered and bent semiconductor channels [16].

The paper is organized as follows: In Sec. II, a brief description of the structure of simulated device is provided. In Sec. III, we give an outline of our device simulation tool. The results of the study and our interpretation of the observed phenomemon are presented in Sec. IV. Finally, we draw our conclusions in Sec. V.

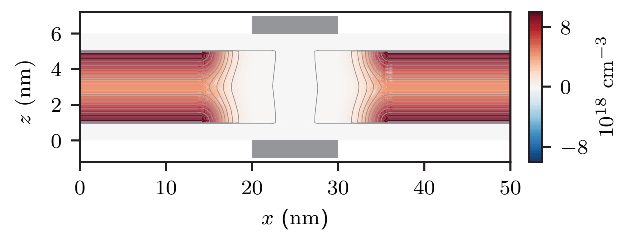

Fig. 1. Net doping profile of the 10 nm UTB DG nMOS that we have studied. The white regions at the top and bottom represent the 1 nm thick gate oxide while the grey patches are used to highlight the position of the gate terminals.

II. Device Description and Simulation of Interface Roughness

We simulate the transport characteristics of a Si (UTB) DG nMOS with channel length of 10 nm (Fig. 1). The device (simulation region) is 4 nm thick (τ_{Si}) and 50 nm long with symmetric 1 nm (EOT $\approx$ 0.3 nm) oxide at each gate. The channel is lightly p-type doped ($\approx 10^{15}$ cm^{-3}), while the highly doped n-type source and drain regions are modeled using a dual Gaussian profile with peaks located at the two oxide-semiconductor interfaces. The device behavior

978-1-5386-6790-3/18/$31.00 ©2018 IEEE

is observed under the application of equal gate bias ($V_{\rm GS}$) at the two gates with a low drain-to-source bias ($V_{\rm DS} \approx 20$ mV). The channel orientation is taken along the [110] direction, following the general trend in VLSI technology.

III. Theoretical Simulation

Our simulation tool solves the two-dimensional (2-D) Schrödinger and Poisson equations self-consistently [18] with *open* boundary conditions over a cross-section of the device. Assuming translational invariance of the doping profile in the out-of-plane direction y for wide devices, our 2-D simulation is a good approximation. The Kohn-Luttinger envelope approximation is used for the Schrödinger equation taking into account the anisotropy of the Si effective masses and the six parabolic conduction band minima. A channel oriented along the [110] direction results in off-diagonal terms in the effective mass tensor. The Schrödinger equation is modified to remove the resulting mixed second-order derivatives, yielding the equation:

$$-\frac{\hbar^2}{2}\left[\frac{1}{m_{\rm x}^v}\frac{\partial^2\phi_\beta^v(x,z)}{\partial x^2}+\frac{1}{m_{\rm z}^v}\frac{\partial^2\phi_\beta^v(x,z)}{\partial z^2}\right]+V(x,z)\phi_\beta^v(x,z) = E_\beta^v\phi^v(x,z)-\frac{\hbar^2k_{\rm y}^2}{2m_{\rm y}^v}\phi_\beta^v(x,z)\ , \quad (1)$$

where $\frac{1}{m_{\rm x}^v}=\frac{1}{2}\left(\frac{1}{m_{\rm tr}^v}+\frac{1}{m_{\rm op}^v}\right)$, $\frac{1}{m_{\rm y}^v}=\frac{1}{m_{\rm x}^v}-\frac{m_{\rm x}^v}{4\left(m_{\rm b}^v\right)^2}$, $\frac{1}{m_{\rm b}^v}=\frac{1}{m_{\rm tr}^v}-\frac{1}{m_{\rm op}^v}$, $\frac{1}{m_{\rm z}^v}=\frac{1}{m_{\rm con}^v}$, and the full (envelope) wavefunction $\psi^v(x,y,z)$ can be written as:

$$\psi_\beta^v(x,y,z)=e^{{\rm i}k_{\rm y}y}\ e^{-{\rm i}\frac{m_{\rm x}^v}{2m_{\rm b}^v}k_{\rm y}x}\phi_\beta^v(x,z)\ . \quad (2)$$

Here $\phi_\beta^v(x,z)$ is the $\beta^{\rm th}$ 2-D wavefunction with energy E_β^v, v is the Si valley index, $m_{\rm tr}$, $m_{\rm con}$ and $m_{\rm op}$ are the effective masses in the transport, confinement and out-of-plane directions, respectively, for Si channel oriented in the [100] direction. $m_{\rm x}^v$, $m_{\rm y}^v$ and $m_{\rm z}^v$ represent the modified effective masses in the transport/channel x, out-of-plane y and confinement z directions, respectively.

Open boundary conditions are used to solve Eq. (1) to ensure interaction of the system with the external environment (electron reservoirs) via leads, enabling us to model system behavior under applied $V_{\rm DS}$. To this end, we follow the QTBM [8], [19] method. The resulting linear system is solved using the second-order centered finite differences method, independently for injection from each lead r. We incorporate a novel way of discretizing the continuous energy spectrum E_β^v of the *open* system by using eigen-energies of the *closed* system Schrödinger Hamiltonian [19], [20]. Our scheme bears resemblance to the method proposed by Fischetti [17]. The calculated wavefunctions are 'box-normalized' and used to determine the electron charge density $n(x,z)$ using the following expression:

$$n(x,z)=\sum_r\sum_v\sum_\beta\sum_{m_r}\frac{1}{\pi\hbar}\sqrt{\frac{m_{\rm y}^v k_{\rm B}T}{2}}|\phi_{m,\beta}^{r,v}(x,z)|^2 \times F_{-\frac{1}{2}}\left(\frac{E_{\rm F}^r-E_\beta^v}{k_{\rm B}T}\right)\ , \quad (3)$$

where $E_{\rm F}$ is the Fermi energy and the index m_r represents traveling modes from lead r injected with energy E_β^v, calculated as part of the QTBM methodology. F_ξ represents the Fermi-Dirac integral of order ξ. Additionally, the hole density is calculated using the following semi-classical expression:

$$p(x,y,z)=\frac{1}{2\sqrt{\pi}}\left(\frac{2m_{\rm h}k_{\rm B}T}{\pi\hbar^2}\right)^{\frac{3}{2}} \times F_{\frac{1}{2}}\left(\frac{V(x,z)-(E_{\rm F}+E_{\rm g})}{k_{\rm B}T}\right)\ , \quad (4)$$

where $m_{\rm h}$ and $E_{\rm g}$ are the hole mass and band gap of Si, respectively.

The different charge distributions, electrons, holes and ionized dopants, are then used to solve the 2-D Poisson equation to generate a 'new' potential which is fed into the Schrödinger equation to form the self-consistent loop. Newton's iteration scheme is used to accelerate the convergence of the self-consistent system. Once convergence is attained, the transport parameters can be extracted from the simulation, as described below.

The transmission coefficient for an electron injected with energy E_β^v from lead r is measured as the ratio of the total transmitted probability-flux to the total flux incident from lead r, integrated over the device cross-section. The 2-D local density of state (LDoS), $\mathcal{D}_{\rm loc}^{r,v}(E,x,z)$, which is basically the spatial variation of the DoS inside the device domain, is calculated by assigning the 2-D electron probability distribution to the corresponding 1-D DoS of the system along the transport direction x:

$$\mathcal{D}_{\rm loc}^{r,v}(E_\beta,x,z)\ =\sum_{m=1}^{N_r}2\sqrt{\frac{2m_{\rm x}^v}{\hbar^2\left(E_\beta^v-E_m^{r,v}\right)}}|\phi_{m,\beta}^{r,v}(x,z)|^2\ . \quad (5)$$

Finally, the total drain current (per unit width of the device in the y direction) is obtained using the following expression [19]:

$$I_{\rm D}=\sum_r\sum_v\sum_\beta\sum_{m_r}\frac{\eta_r e}{2\pi^2\hbar^2}(m_{\rm y}^v m_{\rm x}^v)^{1/2}\frac{\Delta E_\beta^v}{(E_\beta^v-E_{m_r}^{r,v})^{1/2}} \times S_{\rm tot}^r(E_\beta^v,m_r,v)F_{-\frac{1}{2}}\left(E_F-E_\beta^v\right)\ , \quad (6)$$

where $S_{\rm tot}^r(E_\beta^v,m_r,v)$ is the total probability flux, integrated over the device cross-section, entering the device from lead r, $\eta_{r={\rm D}}=-1$ for the drain-to-source term and $\eta_{r={\rm S}}=1$ for the source-to-drain term. The current-density distribution can be similarly calculated by using the probability current at each mesh point, instead of $S_{\rm tot}^r(E_\beta^v,m_r,v)$, in Eq. (6).

IV. Simulation results

Fig. 2 shows the simulated $I_{\rm DS}$-$V_{\rm GS}$ characteristics of a 10 nm DG nMOS at 10 K and 300 K with equal $V_{\rm GS}$ applied at both gates. Characteristic CMOS behavior is observed with fast switching action represented by a low subthreshold slope ($\approx$ 64 mV/dec at 300 K). For device operation deep inside saturation, the charge-distribution plot in Fig. 3(a) shows the occurrence of channel inversion, whereas volume inversion

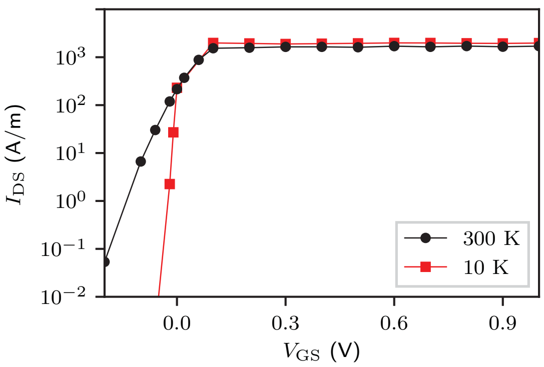

Fig. 2. I_{DS}-V_{GS} characteristics of a 10 nm UTB DG nMOS at 10 K and 300 K. V_{GS} is measured with respect to the flat band voltage of the device. V_{DS} =10 mV.

is observed in the linear region of operation (Fig. 3(b)). The current-density distribution, plotted in Fig. 5(a) for a V_{GS} deep inside saturation, illustrates the path followed by the current. Electrons are injected in a single centered beam at the source (drain), splitting into two when flowing through the inversion channels, to finally merge at the drain (source).

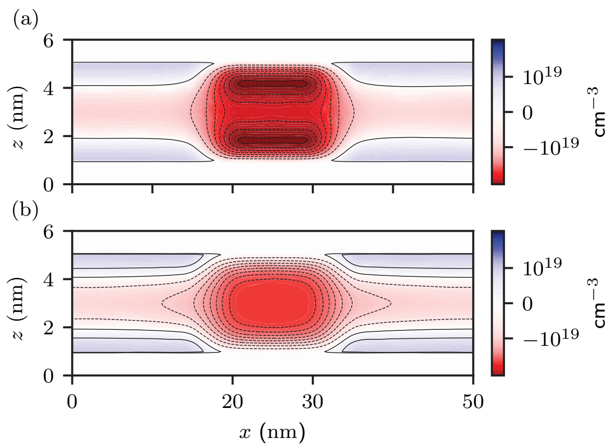

Fig. 3. Total charge distribution in a 10 nm UTB DG nMOS at 300 K. (a) The dark red regions show the creation of two separate inversion channels deep inside saturation, whereas in (b) volume inversion is seen in the linear region of operation. V_{GS}=0.6 V, V_{DS} =10 mV.

Fig. 4 shows the average LDoS distribution along a cross-section of one of the channels and the center of the device for different injection energies (from the source contact). The darker regions exhibit the presence of quasi bound states created within the channel region as a result of the 2-D and field-induced confinement. An interesting feature is the presence of sharp dips in the transmission coefficient (T) observed at these bound-state energies, as shown in Fig. 4(a). Conventionally, a sharp peak in transmission is expected at the resonant energies. On the contrary, the dips in transmission signify occurrence of antiresonances caused by the interaction, or configuration interaction as termed by Fano [9], between quasi-bound states in the channel and the continuum of injected states from the source and drain. To understand the phenomenon qualitatively, we take into consideration Fano's argument [9] which states that waves transmitted at resonating frequencies undergo a phase shift as well as a change of magnitude. Indeed, in the DG nMOS, we observe this resonance for electrons injected into the two degenerate quasi-bound states in the two inversion channels: The two paths undergo opposite phase-shifts that brings them out-of-phase, resulting in destructive interference. Hence we see the antiresonance dips of the transmission probability at the bound-state energies. The fact that antiresonance is seen only in the presence of channel inversion gives further confirmation of our interpretation. Also, as mentioned before in Sec. I, we observe symmetric transmission zeros in our case, contrary to the asymmetric resonance-antiresonance line shapes reported in other studies [11]–[13]. This is because the DG FET structure in saturation mode of operation is analogous to a system of coupled oscillators in which both oscillators (inversion channels in our case) are driven by an external force (V_{DS} in our case), as compared to only one driven oscillator in the latter studies.

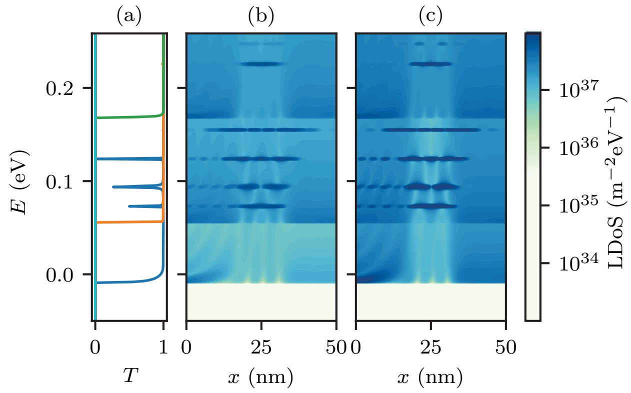

Fig. 4. Transmission coefficient T *vs.* injection energy (a) for current injection from the source contact in a 10 nm UTD DG nMOS at 300 K. The different colored lines correspond to the different injected subbands. The energies are measured with respect to source Fermi level. The LDoS distribution averaged over a cross-sectional thickness of roughly 1.3 nm in the top channel (b) and middle of device (c) at 300 K for injection from the source contact. V_{GS} =1.6 V, V_{DS} =10 mV.

Theoretically, one expects to see drops in the total drain current at those values of the gate bias for which the Fermi level of the device crosses the energy of one of the antiresonance-producing bound states. However, as Fig. 4(a) illustrates, the antiresonance features are extremely sharp and thermal smearing prevents them from appearing in the current-voltage (I-V) characteristics of Fig. 2 at 300 K, and even at 10 K.

Moreover, circulations are seen in the current density resolved for the individual injection energies (from the source contact) at which antiresonance occurs, as illustrated in Fig. 5(b). The even number of vortices, formed as a result of destructive interference, leads to negligible transmission of current at the resonating energies, while momentum conservation forces almost all the electrons to reflect back to

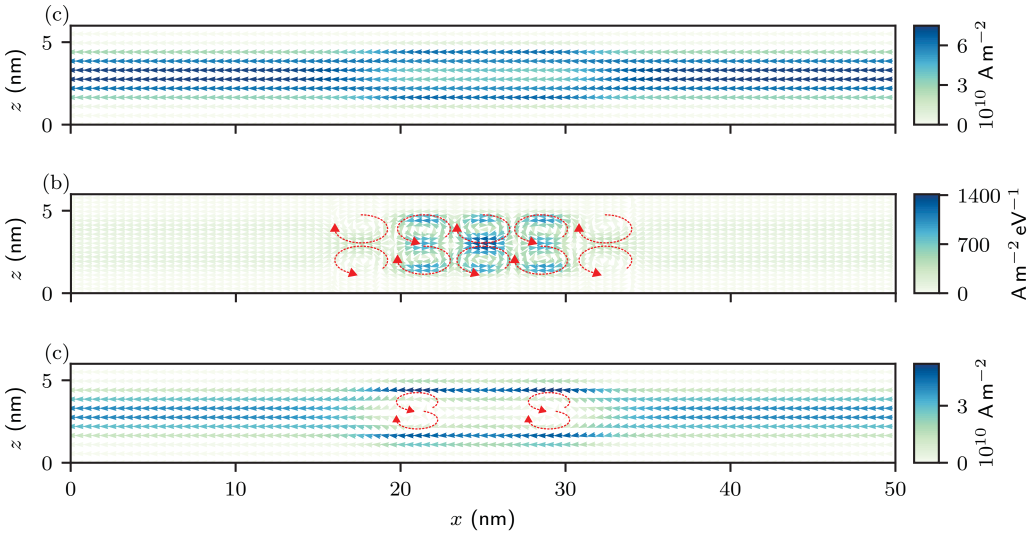

Fig. 5. (a) Current density distribution in a 10 nm UTB DG nMOS at 300 K. (b) Current density distribution resolved for a single injection energy at 300 K. The energy is chosen to have the value at which a sharp dip in transmission occurs due to destructive interference at resonance. V_{GS} =0.6 V, V_{DS} =10 mV. (c) Current density distribution in the same device at 10 K. V_{GS} =0.6 V, V_{DS} =10 mV. The red arrows highlight the direction of the vortices. The plots are stretched to match the aspect ratio of the device.

the injecting lead. It is important to mention here that the total current density at 300 K does not exhibit vortices, while faint vortices persist in the total current density at 10 K, as highlighted in Fig. 5(c). At higher temperatures, the wider energy window resulting from a Fermi Dirac distribution masks the contribution of the resonating states to the total current density.

V. Conclusion

In summary, we have developed a tool to simulate ballistic quantum electron transport in DG FETs and similar devices. The simulated UTB DG nMOS exhibits Fano interference which results in the formation of vortices in the electron current at cryogenic temperatures. Thermal smearing prevents the phenomenon from manifesting itself in the I-V characteristics of the device at higher temperatures. However, we conjecture that this quantum phenomenon can be observed at the macroscopic scale under the right experimental conditions.

References

[1] R. H. Yan, A. Ourmazd, and K. F. Lee, “Scaling the Si MOSFET: from bulk to SOI to bulk”, IEEE Trans. Electron Devices, vol. 39, pp. 1704-1710, Jul. 1992.

[2] F. Balestra *et al.*, “Double-gate silicon-on-insulator transistor with volume inversion: A new device with greatly enhanced performance”, IEEE Electron Device Lett., vol. 8, pp. 410-412, Sep. 1987.

[3] D. J. Frank, S. E. Laux, and M. V. Fischetti, “Monte Carlo simulation of a 30 nm dual-gate MOSFET: how short can Si go?”, 1992 IEDM Tech. Dig., pp. 553-556, Dec. 1992.

[4] J. Saint-Martin *et al.*, “Multi sub-band Monte Carlo simulation of an ultra-thin double gate MOSFET with 2D electron gas”, Semicond. Sci. Technol., vol. 21, pp. L29, Feb. 2006.

[5] R. Granzner *et al.*, “Simulation of nanoscale MOSFETs using modified drift-diffusion and hydrodynamic models and comparison with Monte Carlo results”, Microelectronic Engineering, vol. 83, pp. 241-246, Feb. 2006.

[6] G. Baccarani and S. Reggiani, “A compact double-gate MOSFET model comprising quantum-mechanical and nonstatic effects”, IEEE Trans. Electron Devices, vol. 46, pp. 1656-1666, Aug. 1999.

[7] D. Munteanu *et al.*, “Quantum short-channel compact modelling of drain-current in double-gate MOSFET”, Solid-State Electron., vol. 50, pp. 680-686, Apr. 2006.

[8] C. S. Lent and D. J. Kirkner, “The quantum transmitting boundary method”, J. Appl. Phys., vol. 67, pp. 6353-6359, Jan. 1990.

[9] U. Fano, “Effects of configuration interaction on intensities and phase shifts”, Phys. Rev., vol. 124, pp. 1866-1878, Dec. 1961.

[10] R. C. Bowen, W. R. Frensley, G. Klimeck, and R. K. Lake, “Transmission resonances and zeros in multiband models”, Phys. Rev. B, vol. 52, pp. 2754-2765, Jul. 1995.

[11] M. D. Sturge, H. J. Guggenheim, and M. H. L. Pryce, “Antiresonance in the optical spectra of transition-metal ions in crystals”, Phys. Rev. B, vol. 2, pp. 2459-2471, Oct. 1970.

[12] W. Porod, Z. Shao, and C. S. Lent, “Resonance-antiresonance line shape for transmission in quantum waveguides with resonantly coupled cavities”, Phys. Rev. B, vol. 48, pp. 8495-8498, Sep. 1993.

[13] K. Kobayashi *et al.*, “Fano resonance in a quantum wire with a side-coupled quantum dot”, Phys. Rev. B, vol. 70, pp. 035319, Jul. 2004.

[14] M. L. Ladrón de Guevara, F. Claro, and P. A. Orellana, “Ghost Fano resonance in a double quantum dot molecule attached to leads”, Phys. Rev. B, vol. 67, pp. 195335, May 2003.

[15] M. J. Gilbert and D. K. Ferry, “Vorticity and quantum interference in ultra-small SOI MOSFETs”, IEEE Trans. Nanotechnol., vol. 4, pp. 355-359, May 2005.

[16] S. E. Laux, A. Kumar, and M. V. Fischetti, “Does circulation in individual current states survive in the total current density?”, J. Comput. Electron., vol. 2, pp. 105-108, Dec. 2003.

[17] M. V. Fischetti, “Theory of electron transport in small semiconductor devices using the Pauli master equation”, J. Appl. Phys., vol. 83, pp. 270-291, Jun. 1998.

[18] S. E. Laux, A. Kumar, and M. V. Fischetti, “Analysis of quantum ballistic electron transport in ultrasmall silicon devices including space-charge and geometric effects”, J. Appl. Phys., vol. 95, pp. 5545-5582, Jan. 2004.

[19] P. B. Vyas *et al.*, “Theoretical simulation of negative differential transconductance in lateral quantum nMOS devices”, J. Appl. Phys., vol. 121, pp. 044501, Jan. 2017.

[20] F. Stern, “Self-consistent results for n-type Si inversion layers”, Phys. Rev. B, vol. 5, pp. 4891-4899, Jun. 1972.